ACS APPLIED MATERIALS & INTERFACES

Research Article

www.acsami.org

Perovskite Chromates Cathode with Exsolved Iron Nanoparticles for Direct High-Temperature Steam Electrolysis

Yuanxin Li,[†] Yan Wang,[†] Winston Doherty,[§] Kui Xie,*[,†,‡] and Yucheng Wu*[,†,‡]

[†]Department of Energy Materials, School of Materials Science and Engineering, Hefei University of Technology, No. 193 Tunxi Road, Hefei, Anhui 230009, China

[‡]Key Laboratory of Advanced Functional Materials and Devices, School of Materials Science and Engineering, Hefei University of Technology, No. 193 Tunxi Road, Hefei, Anhui 230009, China

[§]School of Applied Sciences and Engineering, Gippsland Campus, Monash University, Churchill 3842, Victoria, Australia

Supporting Information

ABSTRACT: Recently, composite cathodes based on doped lanthanum chromates have been widely employed for direct steam electrolysis. However, this approach limits the electrode performances and Faraday efficiency due to insufficient electrocatalytic activity. This study addresses the drawbacks and reports an improved electrocatalytic activity and Faraday efficiency of composite cathode with a reversibly exsolved iron nanoparticles anchored on the surface of doped lanthanum chromates. A-site deficient and B-site excess $(La_{0.75}Sr_{0.25})_{0.85}(Cr_{0.5}Fe_{0.5})_{0.85}Fe_{0.15}O_{3-\delta}$ (LSCrFF) was designed as the parent material to anchor the exsolved iron nanoparticles on the surface of perovskite chromate $(La_{0.75}Sr_{0.25})(Cr_{0.5}Fe_{0.5})O_{3-\delta}$ (LSCrF) via high-temperature reduction. The electrical properties of LSCrF and Fe/LSCrF were systematically investigated and correlated with electrochemical performance of the composite electrodes in symmetrical cells and electrolysis cells. The iron nanoparticles significantly improve the electrical conductivity of LSCrF from 1.80 to 6.35 S cm^{-1} for Fe/LSCrF at 800 °C and Po_2 of 10^{-15} atm. The polarization resistance, R_p, of the symmetrical cells was accordingly enhanced from 4.26 Ω cm^2 with LSCrF to 2.58 Ω cm^2 with Fe/LSCrF in hydrogen atmosphere at 800 °C. The Faraday efficiency for the direct steam electrolysis showed a marked increase of 89.3% with LSCrFF cathode at 800 °C and 1.8 V as opposed to 76.7% with the cathodes based on LSCrF. The synergetic effect of catalytic-active iron nanoparticles and redox-stable LSCrF substrate produced improved performances and excellent stability for the direct steam electrolysis without a flow of reducing gas over the composite cathodes.

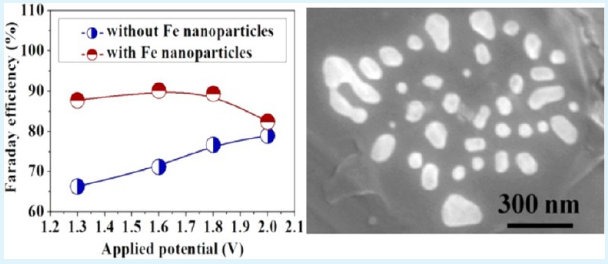

KEYWORDS: *solid oxide electrolyzer, iron nanoparticles, conductivity, doped lanthanum chromates, steam electrolysis*

1. INTRODUCTION

Solid oxide electrolyzer is an electrochemical device for electrolysis with high efficiency and has attracted a great deal of interest in recent years.[1−5] Steam electrolysis is promising due to the high-temperature heat which offers the energy for steam dissociation and accompanied favorable kinetics and thermodynamics. Using external electricity, an oxide-ion conducting solid oxide electrolyzer is able to electrolyze the steam into hydrogen with high efficiency.[6−11]

Currently, numerous experiments have focused on the preferential use of Ni-YSZ cermets for the cathode of the oxide-ion conducting solid oxide electrolyzer in high-temperature steam electrolysis. However, the Ni-YSZ cermet is not redox-stable and requires a significant concentration of reducing gas flowing over Ni to prevent its oxidation to NiO, which in turn would cause a loss of electrical conductivity and even failure of electrodes.[12,13] In recent years, the perovskite doped lanthanum chromates have been favored to address these drawbacks due to its reported activity and unique redox-stable capabilities.[14,15] Consequently, its use has attracted a lot of attention in the high-temperature SOFC field. The perovskites based on $LaCrO_3$, for example $(La_{1-x}Sr_x)(Cr_y, M_{1-y})O_{3-\delta}$ (M = Mn, Fe, Ti, Co), have been proven to be promising anode materials for solid oxide fuel cell and have eventually led to the materials receiving a great deal of attention in the field of cathodes for high-temperature solid oxide electrolyzer.[16−21] These ceramic materials can be used both as cathodes and anodes[19−21] and function well under oxidizing and reducing conditions. A proper amount of deficiency and doped atoms are utilized for designing materials as critical tools;[16] however, it is important that the materials keep redox reversible and stable structure with intact optimal conductivity and electrocatalytic properties.

Recently, we demonstrated that the direct electrolysis of CO_2 could produce CO and O_2 in an oxide-ion conducting solid oxide electrolyzer based on doped lanthanum chromates

Received: May 26, 2013
Accepted: August 9, 2013
Published: August 9, 2013

   dx.doi.org/10.1021/am4020132 | ACS Appl. Mater. Interfaces 2013, 5, 8553−8562

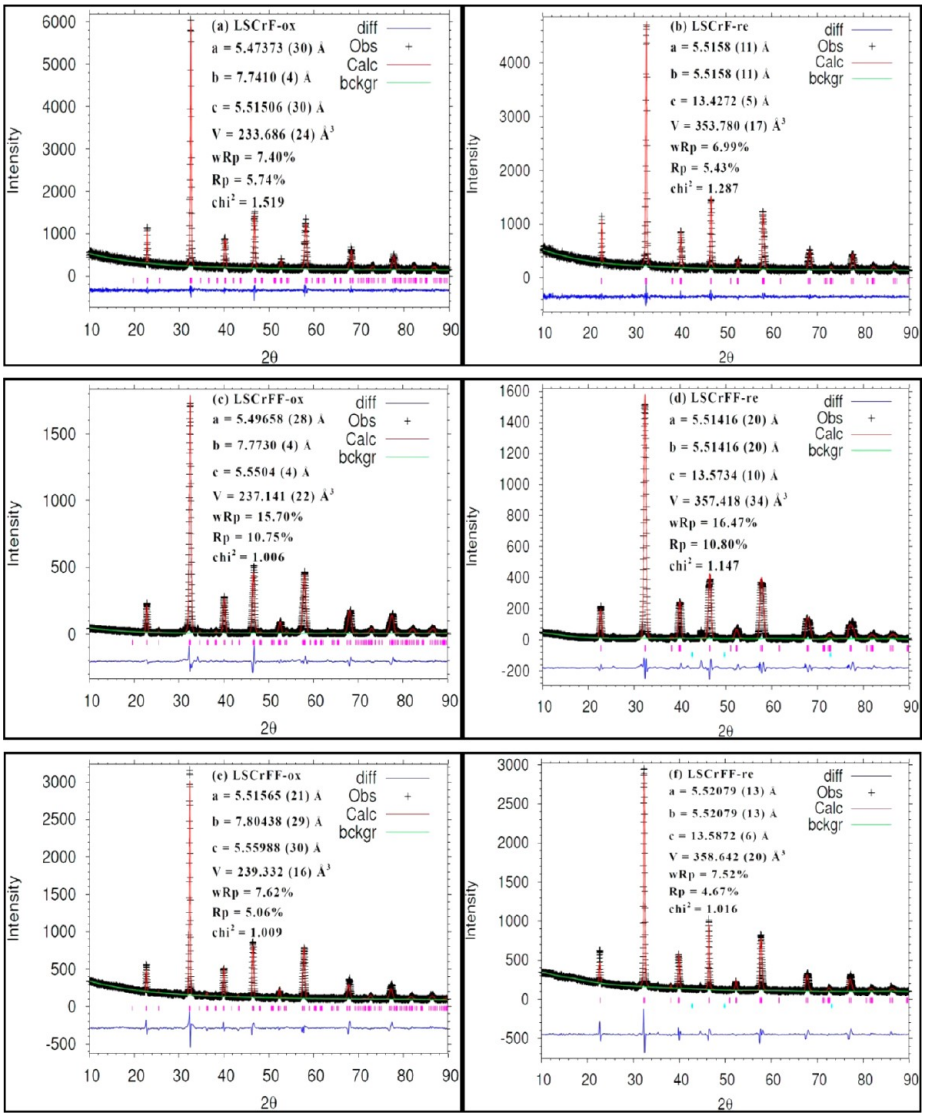

Figure 1. Rietveld refinement patterns of LSCrF and LSCrFF powers: (a and c) oxidized and (b and d) reduced. LSCrFF powers after three redox cycles: (e) oxidized and (f) reduced.

electrode without the flow of reducing gas over it. However, the catalytic activity of the ceramic materials may be a constraint on the improvement of their catalytic performance. The Faradic current efficiency is restricted by the insufficient electrocatalytic activity of the LSCM ceramic cathode.[20,21] In order to enhance the electrode performances, nanosized iron particles were loaded onto the composite cathode for the direct steam electrolysis in an oxide-ion-conducting solid oxide electrolyzer as reported in our previous work.[20] However, a decrease of approximately 20% was observed after running the direct steam electrolysis for 15 h, which is attributed to the agglomeration of iron nanoparticles that degrades the electrocatalytic activity of the composite cathode. Therefore, it is necessary to improve the iron nanoparticles/ceramic substrate interfaces to prohibit the agglomeration of nanoparticles. This is expected to enhance the electrode kinetics without impairing the electrocatalytic activity of the high-temperature steam electrolysis.

So far, a great deal of efforts have been devoted to the study of advanced catalytic-active cathodes based on doped lanthanum chromates for solid oxide electrolyzer, but there still exist scientific challenges for its developments. Perovskite, $La_{0.75}Sr_{0.25}Cr_{0.5}Fe_{0.5}O_{3-\delta}$, has been reported as a high-temperature electrocatalytic heterogeneous catalyst with reasonable catalytic properties and redox stability. However, the experimental configuration was far from optimal. In this study therefore, perovskite-type $(La_{0.75}Sr_{0.25})_{0.85}(Cr_{0.5}Fe_{0.5})_{0.85}Fe_{0.15}O_{3-\delta}$ with A-site deficiency and B-site excess was designed to anchor a composite nanosized iron/$(La_{0.75}Sr_{0.25})(Cr_{0.5}Fe_{0.5})O_{3-\delta}$ (Fe/LSCrF) through a reversible exsolution of iron nanoparticles onto the surface of LSCrF via a treatment in a high-temperature reducing atmosphere. The anchored interface is expected to enhance the electrocatalytic kinetics and the high-temperature stability of iron nanoparticles. The electrical properties of the oxidized and reduced LSCrF and LSCrFF were systematically studied and further correlated with the electrochemical performance of the composite electrodes in symmetrical cells or electrolysis cells. Steam electrolysis with cathodes based on LSCrF and LSCrFF were investigated in solid oxide electrolyzers with or without reducing gas flowing over the cathodes, respectively.

dx.doi.org/10.1021/am4020132 | ACS Appl. Mater. Interfaces 2013, 5, 8553−8562

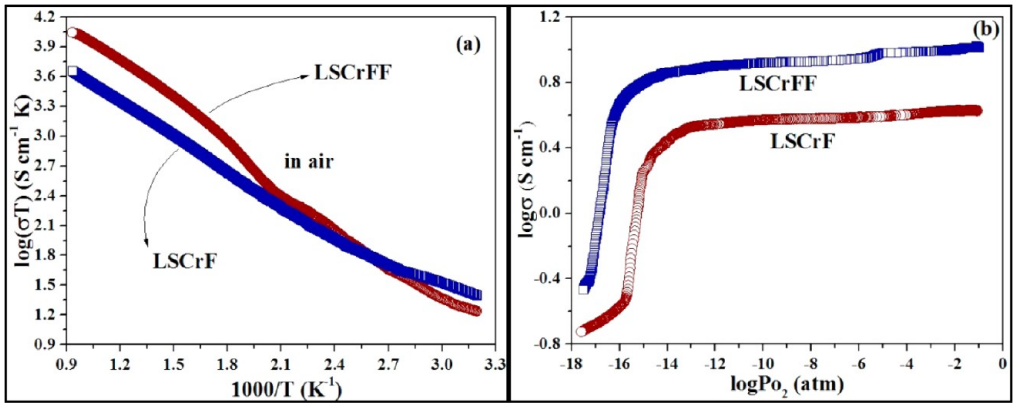

Figure 2. Total conductivity of LSCrF and LSCrFF: (a) in air and (b) versus oxygen partial pressure.

2. EXPERIMENTAL SECTION

All chemicals used in this current investigation were of analytical grade unless otherwise specified. All the chemicals in our experiment were purchased from SINOPHARM Chemical Reagent Co., Ltd. (China) and used as received without further purification. The LSCrF and LSCrFF were synthesized by a solid state reaction method in which the powders of La_2O_3, $SrCO_3$, Cr_2O_3, and Fe_2O_3 were mixed together, ball-milled for 15 min, dried, then pressed into pellets and fired at 1400 °C for 10 h in air.[22,23] XRD (Cu K_α, D/MAX2500 V, Japan) was performed to identify the phase formation (0.02° min^{-1}). The 1-mm-thick 8YSZ electrolyte supports were fabricated by dry-pressing 8YSZ powders into green disks with a diameter of ~20 mm and then fired at 1500 °C for 10 h.[24−29] Proper amounts of LSCrF and LSCrFF powders were pressed into bars and fired in air at 1400 °C for 2 h to obtain samples for conductivity tests. The relative densities of the sample LSCrF and LSCrFF reached about 85.6% and 91.1%, respectively. High sintered density is good for improving the conductivity, and the anchored Fe nanoparticles are also expected to improve both the mixed conductivity and the electrocatalytic activity of the electrode. The conductivity tests were performed with temperature ranging from 50 to 800 °C in air and 5% H_2/Ar using a multimeter (Keithley 2000). The oxygen partial pressure ($0.1-10^{-18}$) was controlled by flowing 5% H_2/Ar and simultaneously recorded with an online oxygen sensor (Noveltech Type 1231, Australia). The prepared LSCrF and YSZ powders (50:50 wt %) were mixed with ethyl cellulose-terpineol to form a slurry and then printed onto the two surfaces of YSZ discs to assemble symmetrical cells with the configuration of (LSCrF-YSZ/YSZ/LSCrF-YSZ and LSCrFF-YSZ/YSZ/LSCrFF-YSZ). Solid oxide electrolyzers with the configuration of ((cathode) LSCrF-YSZ/YSZ/LSM-YSZ (anode) and ((cathode) LSCrFF-YSZ/YSZ/LSM-YSZ (anode)) were assembled in the similar way followed by a heat treatment at 1100 °C for 3 h in air. The silver paste (SS-8060 Xinluyi, China) was printed onto the electrode surface and used for current collection after a heat treatment at 550 °C for 30 min. The single solid oxide electrolyzer was sealed to a homemade testing jig by using ceramic paste (JD-767, Jiudian, China) for systematical electrochemical measurements at 800 °C.

Alternating current impedance spectroscopies of the two kinds of symmetrical cells were tested as a function of hydrogen partial pressure in two-electrode mode at 800 °C using an electrochemical station (IM6, Zahner, Germany) with a frequency range of 4 M−0.1 Hz. Silver paste and silver electrical wires were used for current collection and the external circuit, respectively, as discussed above. The hydrogen partial pressure is controlled by mixing different ratios of H_2 and Ar using mass flow meters (D08-3F, Sevenstar, China). The sample was first tested with H_2 and later with Ar, which is beneficial to the exsolution of Fe nanoparticles from the A-site deficient and B-site excess LSCrFF. Scanning electron microscope (SEM; JSM-6490LV, JEOL Ltd., Japan) and X-ray photoelectron spectroscopy (XPS; ESCALAB25, Thermo) were employed to characterize the materials before and after high-temperature reduction. In the process of steam electrolysis, cathodes of solid oxide electrolyzer (two types) were fed with 3% H_2O/4.93% H_2/Ar and 3% H_2O/Ar with anodes in static air, respectively. The solid oxide electrolyzers were sealed to an alumina tube in which the steam is input for electrolysis in the experimental setup. The electrochemical tests were performed in a two-electrode mode. The current−voltage ($I-V$) curves of the solid oxide electrolyzers were obtained. Direct electrolysis of steam in the solid oxide electrolyzer based on LSCrF and LSCrFF were performed with different potential loads. The output gas from the cathodes was analyzed with an online gas chromatograph (GC9790II, F.L., China).

3. RESULTS AND DISCUSSION

3.1. Structure. Figure 1a,c shows the XRD Rietveld refinement patterns of the prepared LSCrF and LSCrFF powders (LSCrF-ox and LSCrFF-ox) in air, and Figure 1b,d accordingly represents the profiles for the powders reduced (LSCrF-re and LSCrFF-re) in 5% H_2/Ar for 3 h at 800 °C. The experimental and calculated results indicated perovskite structure with space group *Pnma* for oxidized samples and $R\bar{3}c$ (167) for reduced samples, which is consistent with reported data in previous studies.[30] A strong peak ($2\theta = 44.6°$), which is the strongest (110) diffraction peak of iron in relation to the exsolution of the iron metal phase from LSCrFF with A-site deficiency and B-site excess, was observed in Figure 1d. Slight exsolution of iron metal was also observed in reduced LSCrF; however, the perovskite structure with space group $R\bar{3}c$ (167) was retained, suggesting the excellent red-ox stability of the parent material, even though the doped metal was exsolved from lattice to anchor on the LSCrF surface. The slight difference of cell parameters for oxidized and reduced samples, as detailed in Figure 1, is due to the transition of Cr^{6+} to Cr^{3+}, $^{4+}$, and Fe^{4+} first to Fe^{3+} and later to Fe after reduction. Figure 1e,f shows the XRD profiles of the LSCrFF after three red-ox cycles. The iron particles integrated back to the LSCrF lattice to form a single LSCrFF phase can be seen in Figure 1e. However, the exsolution is repeatedly achieved when the sample was again reduced as revealed in Figure 1f, suggesting a reversible exsolution of iron particles in the redox-reversible cycles between LSCrFF and Fe/LSCrF composites.

3.2. Conductivity. In order to study the electrical properties of LSCrF and LSCrFF, conductivity tests were carried out both in air against temperature (50−800 °C) and oxygen partial pressure (Po_2) at 800 °C. The LSCrF and LSCrFF are p-type electronic conductors as evident in Figure 2a. The temperature dependence of conductivity shows a typical semiconducting behavior having a positive coefficient with temperature up to 800 °C in air. The conductivity of the

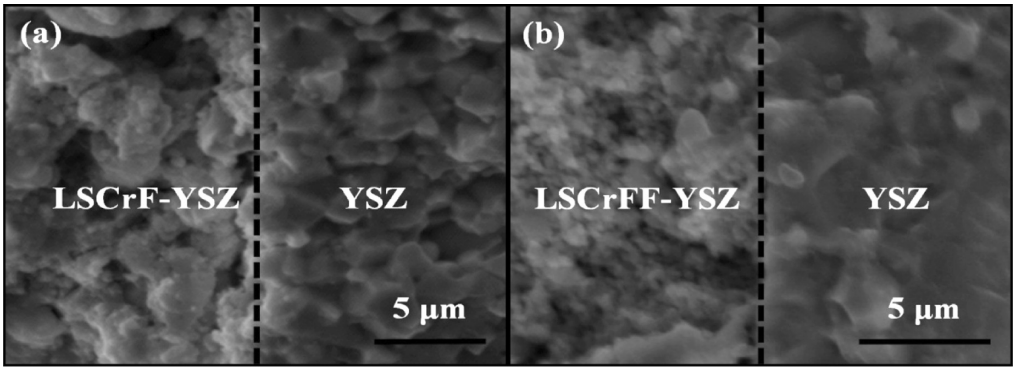

Figure 3. Cross-sectional views of the symmetrical cells based on LSCrF and LSCrFF electrodes.

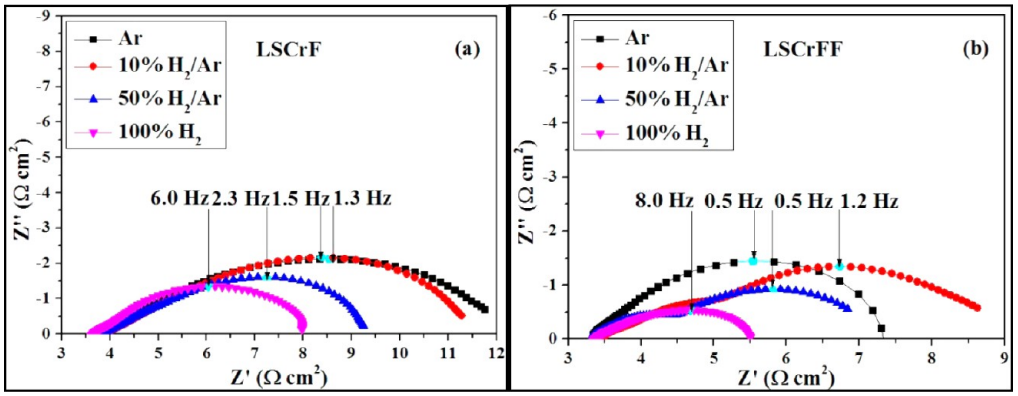

Figure 4. ac impedance spectroscopy of YSZ-supported symmetrical cells based on LSCrF and LSCrFF electrodes at different hydrogen partial pressure.

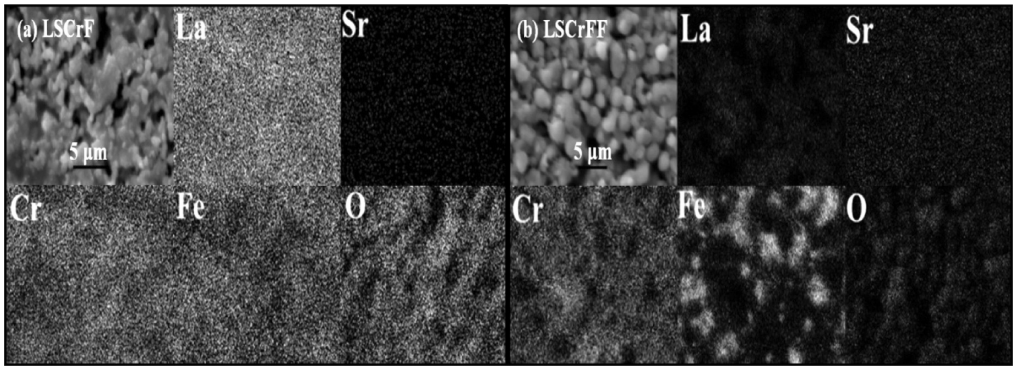

Figure 5. SEM micrographs and EDS maps of LSCrF and LSCrFF oxidized at 1100 °C and reduced in 5% H_2/Ar at 800 °C.

LSCrF reached an optimum at 4.24 S cm^{-1} at a temperature of 800 °C and activation energy (ΔE) of 9.08 kJ mol^{-1}. The p-type conducting properties are as shown in Figure 2b, where the conductivity of the LSCrF sample is approximately 1.80 S cm^{-1} at 800 °C and does not depend on the oxygen partial pressure at Po_2 above 10^{-15} atm. However, a steady but significant decrease in conductivity was observed with Po_2 below 10^{-15} atm to 0.19 S cm^{-1} at 10^{-18} atm and 800 °C. This is probably attributed to the decrease in the concentration of the charge carrier in reducing atmospheres. Evidently, the conductivity of LSCrF ceramics is greatly influenced by oxygen partial pressure in strong reducing atmospheres. On the other hand, the perovskite LSCrFF with A-site deficiency and B-site excess demonstrated higher conductivity both in air and 5% H_2/Ar. The conductivity of the LSCrFF reaches approximately 10.35 S cm^{-1} at 800 °C with the activation energy (ΔE) of 11.38 kJ mol^{-1} in air. Although, similar behavior of the dependence of conductivity on the oxygen partial pressure was observed; however, at 800 °C, the conductivity reaches 6.35 and 0.34 S cm^{-1} at Po_2 of 10^{-15} and 10^{-18} atm, respectively. The conductivity of LSCrFF is strongly enhanced due to excellent electrocatalytic activity of the iron nanoparticles anchored on the LSCrF surface, as a result of which the mixed conductivity increases in reducing atmospheres.

3.3. Symmetrical Cell. Figure 3a,b presents the microstructure of the 1-mm-thick YSZ electrolyte-supported symmetrical cells with LSCrF and LSCrFF electrodes, respectively. The YSZ is uniform and dense, and the two porous cathodes with a thickness of ~12 μm adhere to the electrolyte very well. The ac impedance spectroscopies of symmetrical cells with electrodes based on LSCrF and LSCrFF reduced in 5% H_2/Ar were carried out versus hydrogen partial pressure at 800 °C and

dx.doi.org/10.1021/am4020132 | ACS Appl. Mater. Interfaces 2013, 5, 8553−8562

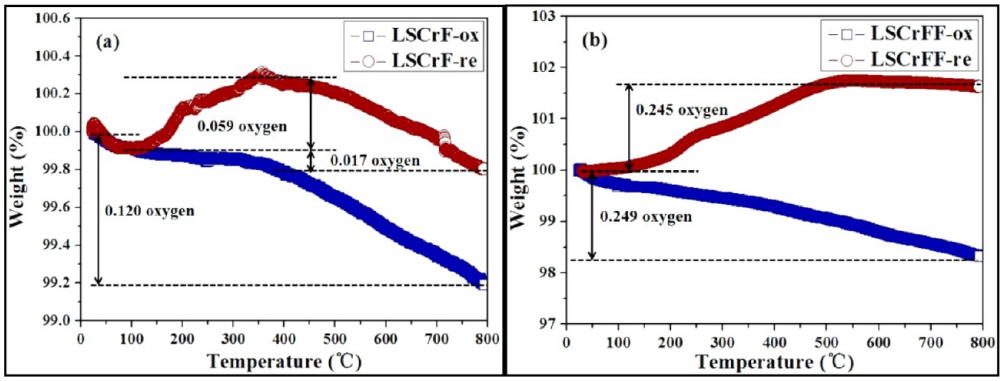

Figure 6. TGA tests of oxidized and reduced (a) LSCrF and (b) LSCrFF in air from 25 to 800 °C at the rate of 5° min^{-1}.

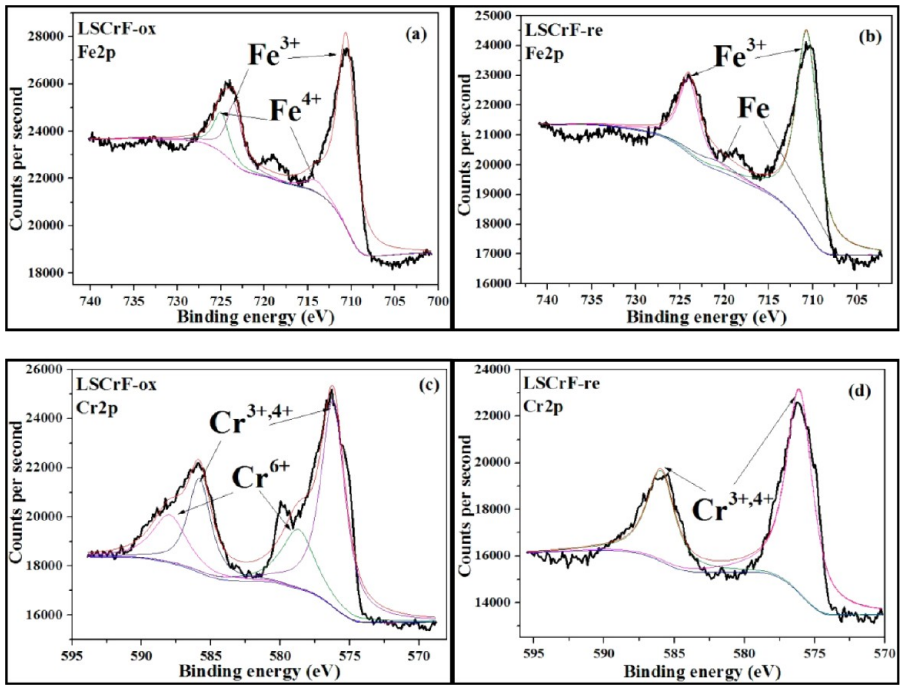

Figure 7. Cr_{2p}, Fe_{2p} X-ray photoelectron spectroscopy of LSCrF: oxidized at 1100 °C and reduced at 1100 °C.

displayed in Figure 4. The polarization resistance (R_p) decreased with increasing hydrogen partial pressure whereas the series resistance (R_s) is generally stable in a wide range of hydrogen partial pressure. The decrease in conductivity of LSCrF and LSCrFF in stronger reducing atmosphere, as previously discussed, is expected to lead to an increase in R_p. However, a considerable improvement of R_p was observed from the ac impedance spectroscopy at higher hydrogen partial pressure, which indicates that the stronger reducing atmosphere significantly activates the electrodes, enhances the electrocatalytic activity, and thus decreases the electrode polarization resistances. The R_p of the symmetrical cell is 4.26 Ω cm^2 for LSCrF in pure hydrogen but improved to 2.58 Ω cm^2 for LSCrFF. This may be attributed to the improved electrocatalytic activity of the Fe/LSCrF matrix. On the other hand, the enhanced conductivity of Fe/LSCrF would be further favorable for the electrode polarizations.

3.4. Metal Exsolution. Figure 5 shows the SEM micrographs and energy-dispersive X-ray spectroscopy (EDS) maps of LSCrF and LSCrFF taken from the reduced pellets. The sintered samples were reduced in 5% H_2/Ar at 800 °C and oxidized in air at 1100 °C for three cycles with their relative densities reaching 85.1% and 90.2%, respectively. It was found that the iron element is homogeneously dispersed in the reduced LSCrF, as shown in Figure 4a, and the other elements are also well distributed in the bulk, indicating that no large amount of iron nanoparticles were exsolved from LSCrF even in an extremely reducing atmosphere. In contrast, the exsolution of iron nanoparticles were observed from the SEM and EDS of the reduced LSCrFF (Fe/LSCrF). The presence of Fe nanoparticles were confirmed by SEM and EDS in addition to XRD as discussed above. The result indicates that the reversible exsolution of metal nanoparticles is feasible in strongly defected perovskite. The dispersed iron nanoparticles anchoring on the LSCrF surface are expected to prohibit the agglomeration and improve the electrocatalytic activity of the composite cathode for high-temperature steam electrolysis.

Titration techniques and thermogravimetry (TGA) are more commonly used for the analysis of oxygen nonstoichiometry. The TGA tests in air were conducted using the oxidized and reduced LSCrF and LSCrFF samples, and results are given in parts a and b of Figure 6, respectively. The loss of oxygen for

dx.doi.org/10.1021/am4020132 | ACS Appl. Mater. Interfaces 2013, 5, 8553−8562

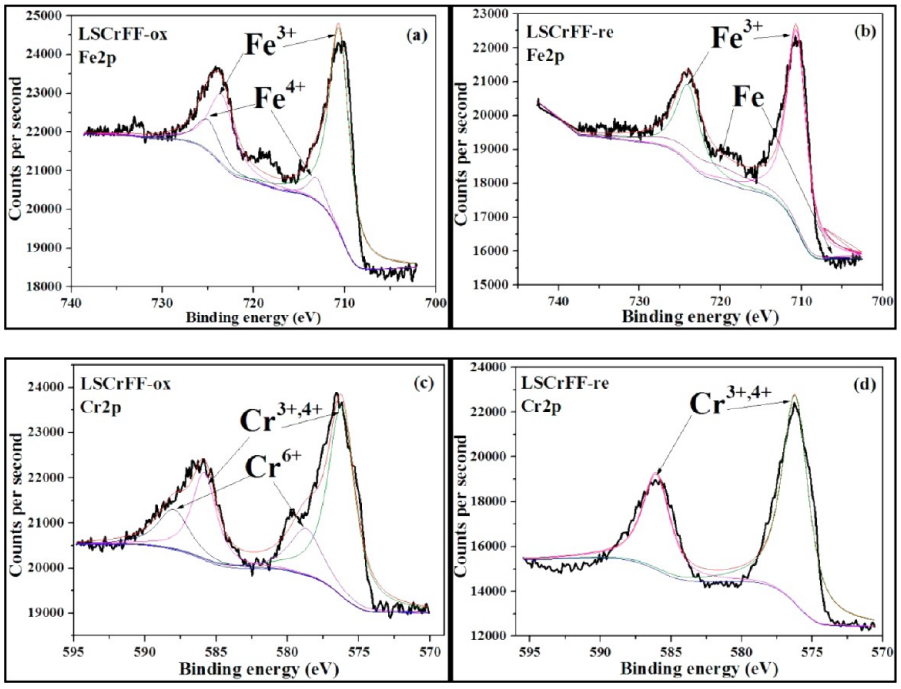

Figure 8. Cr_{2p}, Fe_{2p} X-ray photoelectron spectroscopy of LSCrFF: oxidized at 1100 °C and reduced at 1100 °C.

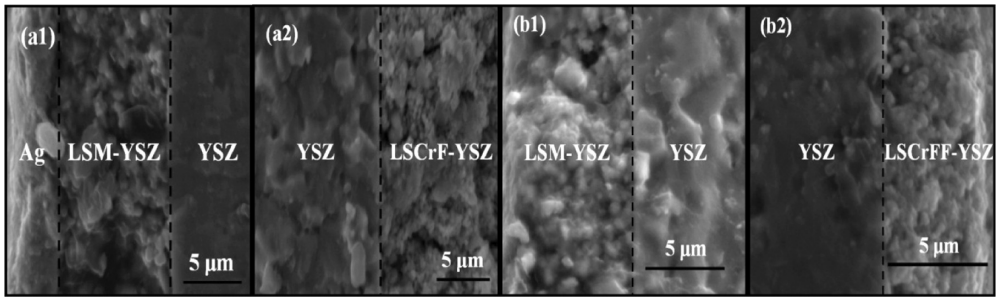

Figure 9. Cross-sectional SEM micrographs for solid oxide electrolyzers of (a1) Ag/LSM-YSZ/YSZ, (a2) LSCrF-YSZ/YSZ and (b1) LSM-YSZ/YSZ, (b2) LSCrFF-YSZ/YSZ.

oxidized LSCrF per perovskite unit (ABO_3) is 0.120 (0.805 wt %), while it is 0.249 (1.669 wt %) for oxidized LSCrFF at 800 °C. In contrast, the weight of reduced LSCrF decreases to 0.085 wt % at ∼100 °C, which may relate to the absorbed water and other gas, and then increases to 0.309 wt % at ∼400 °C due to the reoxidation of reduced LSCrF. The weight increase (1.638 wt %) of LSCrFF includes two processes: the reoxidation of LSCrF and iron. The results indicate that the increase of 1.329 wt % is due to the reoxidation of iron, which is consistent with the weight change of the chemical reaction: LSCrF + Fe → LSCrFF.

To describe the different chemical state of the samples, core level spectroscopies including Fe_{2p} and Cr_{2p} for the oxidized and reduced LSCrF and LSCrFF were obtained using XPS as shown in Figures 7 and 8, respectively. All XPS spectroscopies were fitted with a Shirley-type background subtraction method. The background-functions for different spectroscopies of elements were fitted by 80% Gaussian and 20% Lorenz. Figure 7a shows the Fe_{2p} core-level XPS spectroscopy of the oxidized LSCrF sample, in which the spin−orbit splitting in the Fe_{2p} XPS spectroscopy shows a double of $2p_{1/2}$ and $2p_{3/2}$ excitation. The Fe^{3+} ($2p_{1/2}$) and Fe^{4+} ($2p_{1/2}$) peaks are observed at 723.46 and 724.97 eV, whereas Fe^{3+} ($2p_{3/2}$) and Fe^{4+} ($2p_{3/2}$) show peaks at 710.59 and 714.08 eV respectively. The XPS data revealed Fe^{3+}/Fe^{4+} atomic ratios to be approximately 83.6:16.4 for LSCrF and 84.2:15.8 for LSCrFF. The Fe^{3+} is the main chemical state of iron element for the reduced LSCrF and LSCrFF as evident in Figures 7b and 8b. In these Figures, the Fe^{3+} ($2p_{1/2}$) and Fe ($2p_{1/2}$) peaks were observed at 723.99 and 720.98 eV, with Fe^{3+} ($2p_{3/2}$) and Fe ($2p_{3/2}$) occurring at 710.64 and 706.01 eV, respectively. This further confirms that the iron metal is exsolved from the reduced samples. Most of the Fe^{4+} is reduced to either Fe^{3+} or Fe, and as a consequence, significantly lowers the concentration of charge carrier, $h^{\bullet}$, and further decreases the conductivity in stronger reducing atmospheres. The Fe/Fe^{3+} atomic ratio is ∼6.6:93.4 for LSCrF as confirmed by the XRD result, indicating that the tiny amount of metal iron is still exsolved from LSCrF under reducing conditions and this is in good agreement with the XRD results. In contrast, the Fe/Fe^{3+} atomic ratio reaches as high as 19.8:80.2 for reduced LSCrFF, implying that a large amount of iron nanoparticles were exsolved to anchor on the surface of LSCrF to form Fe/LSCrF composite as validated by the XRD, SEM, and EDS results.

Figures 7c and 8c display the Cr_{2p} core-level XPS spectroscopies of oxidized LSCrF and LSCrFF samples, in

dx.doi.org/10.1021/am4020132 | ACS Appl. Mater. Interfaces 2013, 5, 8553−8562

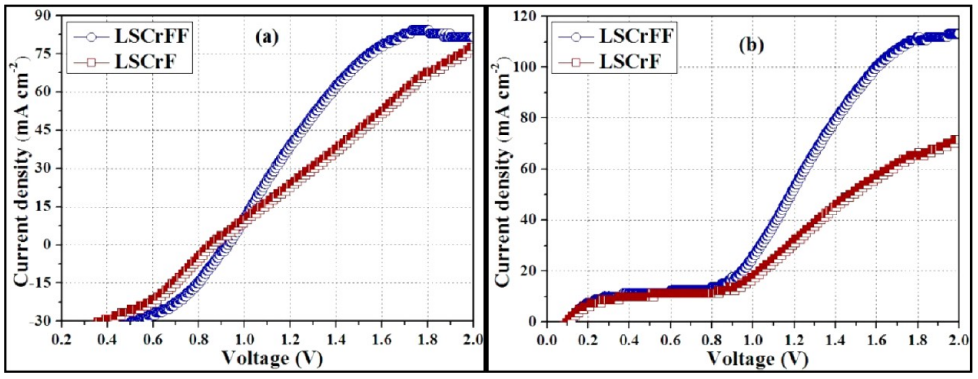

Figure 10. Current−voltage curves of the solid oxide electrolyzers with cathodes based on LSCrF and LSCrFF fed with (a) 3% H_2O/4.93% H_2/Ar and (b) 3% H_2O/Ar at 800 °C, respectively.

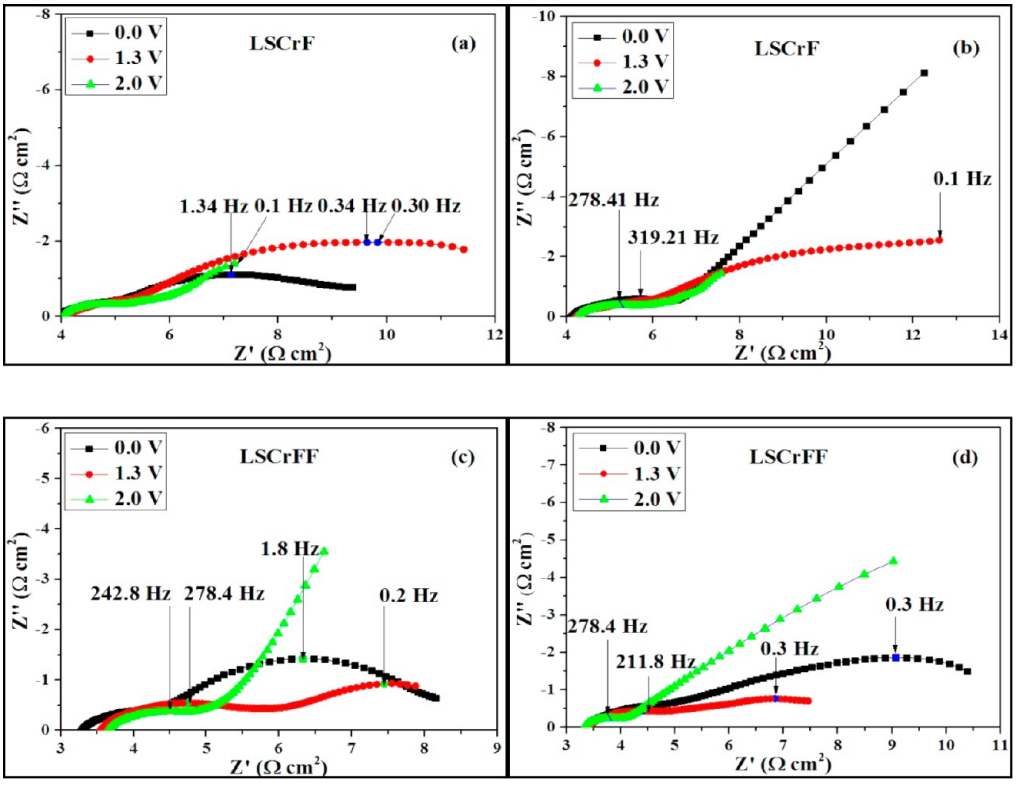

Figure 11. In situ ac impedance spectroscopy of solid oxide electrolyzers with cathodes based on LSCrF and LSCrFF fed with (a and c) 3% H_2O/4.93% H_2/Ar; (b and d) 3% H_2O/Ar at 800 °C.

which the spin−orbit splitting in the Cr_{2p} XPS spectroscopy shows a double of $2p_{1/2}$ and $2p_{3/2}$ excitation. The Cr^{3+} ($2p_{1/2}$) and Cr^{6+} ($2p_{1/2}$) peaks are observed at ∼585.83 and 587.98 eV, whereas ∼576.21 and 578.70 eV are peaks of Cr^{3+} ($2p_{3/2}$) and Cr^{6+} ($2p_{3/2}$), respectively. The weak signal of Cr^{4+} is observed at about 576.10 eV; however, it is difficult to distinguish peaks of Cr^{3+} from Cr^{4+} due to their close binding energy and low contents of Cr[4]. For oxidized samples, the Cr^{3+}/Cr^{6+} ratio is ∼66.3:33.7 for LSCrF and ∼72.2:27.8 for LSCrFF from the XPS data. In contrast, Cr^{3+} is the main chemical state for reduced LSCrF and LSCrFF samples as can be seen in Figures 7d and 8d. The Cr element in the B site has a positive effect on the stability of perovskite structure in an oxidizing atmosphere. Since Cr^{3+} is the main chemical state, even in a strong reducing atmosphere, most Cr^{6+} is reduced to Cr^{3+}, which may decrease the concentration of cationic defects caused by the egression of lattice Fe as metallic nanoparticles. It is worth noting that Cr^{3+} is ∼70% before being reduced, implying that the +3 chemical state of Cr is generally stable and thus contributes to the stability of the LSCrFF.

3.5. Steam Electrolysis. Figure 9 presents the microstructures of the solid oxide electrolyzers with the configurations of (cathode) LSCrF-YSZ/YSZ/LSM-YSZ (anode) and (cathode) LSCrFF-YSZ/YSZ/LSM-YSZ (anode), respectively. The silver current collection layer is around 5 μm in thickness, and the porous cathode and anode layers are approximately 12 μm in thickness, which adhere well to the 1-mm-thick YSZ electrolyte. Figure 10 corresponds to the $I-V$ curves of solid oxide electrolyzers at 800 °C with titled cathodes in 3% H_2O/4.93% H_2/Ar and 3% H_2O/Ar, respectively. The open circuit voltages (OCV) of the solid oxide electrolyzer reach approximately 0.997 V with the LSCrF cathode and 0.988 V

dx.doi.org/10.1021/am4020132 | ACS Appl. Mater. Interfaces 2013, 5, 8553−8562

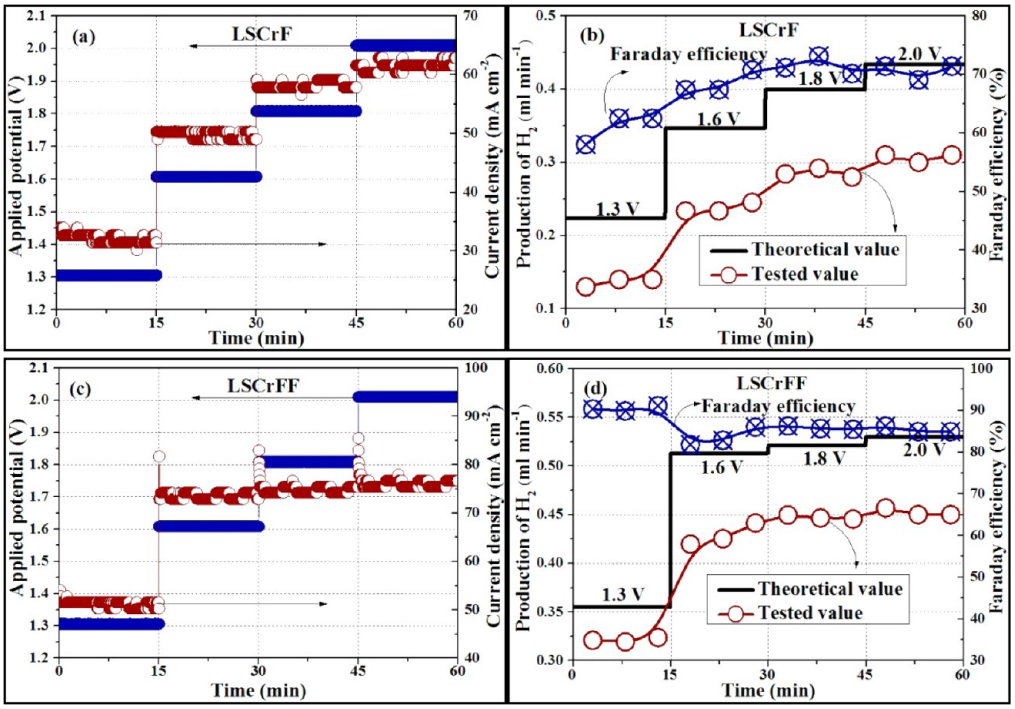

Figure 12. Electrolysis performance of the solid oxide electrolyzers with cathodes based on LSCrF and LSCrFF at different applied potentials of 1.3 V, 1.6 V, 1.8 V, and 2.0 V in 3% H_2O/4.93% H_2/Ar at 800 °C.

with the LSCrFF cathode in 3% H_2O/4.93% H_2/Ar. This is much lower, as observed from the $I-V$ curves, compared to the theoretical value of 1.180 V for 3% H_2O/4.93% H_2/Ar calculated from the Nernst equation and may probably be attributed to the less than perfect process of the $I-V$ test. On the other hand, it seems that the low OCV value in the test might be attributed to the slight gas leakage at the cathode as the ceramic paste is being utilized to ensure it is properly sealed. It is apparent that the thinner and simpler electrode structure performs better for ionic conduction at the electrode and electrolyte interface. The decrease in current densities observed for the cell based on LSCrFF at a voltage above 1.8 V may be due to the local starvation of steam at high voltages. The $I-V$ curves are far from linear with a slope change at approximate 1.0 V, which indicates that two different electrochemical processes are present in the two voltage regions: the electrochemical reduction of cathodes at low voltages and the steam electrolysis at high voltages. The onset of steam electrolysis might be anticipated at approximately 1.0 V in the $I-V$ curves.

The current density at around 1.5 V is generally ~58.3% and ~75.6% larger with Fe/LSCrF than that of the cell with LSCrF in 3% H_2O/4.93% H_2/Ar and 3% H_2O/Ar, respectively. Apparently, the exsolution of iron nanoparticles significantly enhances the electrocatalytic performance of the cathodes based on Fe/LSCrF and therefore improves the electrode polarizations. It should be noted that, as shown in Figure 10b, the cell based on Fe/LSCrF still demonstrates better performance even in 3% H_2O/Ar without flowing reducing gas over the electrode. The synergetic effect of catalytic-active iron and redox-stable LSCrF leads to excellent stability and better cathode performance for the direct steam electrolysis in an oxide-ion conducting solid oxide electrolyzer.

In order to study the change of R_s and R_p in situ, ac impedance spectroscopies of solid oxide electrolyzers (LSCrF-YSZ/YSZ/LSM-YSZ and LSCrFF-YSZ/YSZ/LSM-YSZ) were carried out with cathodes in 3% H_2O/4.93% H_2/Ar and 3% H_2O/Ar. As shown in Figure 11, the R_s values are ~4.1 Ω cm^2 for the cells based on LSCrF and ~3.5 Ω cm^2 for LSCrFF, which might be due to the enhancement of electrode/electrolyte interfaces with the exsolved iron nanoparticles. The R_p of the cells based on LSCrF and LSCrFF cathodes changes considerably as applied voltages increase from 0 to 2.0 V in 3% H_2O/4.93% H_2/Ar and 3% H_2O/Ar. This may be attributed to the fact that the increased voltage significantly activated the electrodes and led to a remarkable decrease in R_p. There exists two primary electrochemical processes in the voltage range of 0 to 2 V during the steam electrolysis process: reduction of the LSCrF and LSCrFF cathodes and steam electrolysis. The reduction of the LSCrF and LSCrFF cathodes is the main process below 1.0 V, and the steam electrolysis dominates the electrolysis process at higher voltages because the electrochemical potential of $2H_2 + O_2 \rightarrow 2H_2O$ is approximately 1.0 V at 800 °C. At this stage, the R_s value dominates the total cell performance at higher voltage, which indicates that the ionic transport in the YSZ electrolyte is the limiting step in the cell process. The electrochemical reduction of the cathodes is the main process below 1.0 V, and the steam electrolysis is expected to be the dominating process above 1.0 V; however, the electrochemical reduction of the LSCrF and LSCrFF cathodes still exist at higher voltages.

The impedance spectroscopy consists of the high-frequency and low-frequency semicircles. The high-frequency arcs (R_1) are mainly due to the gas diffusion and charge transfer at cathodes/YSZ interfaces. The R_1 is 1.15 Ω cm^2 for a cell based on LSCrF and 1.46 Ω cm^2 for a cell based on LSCrFF in 3% H_2O/4.93% H_2/Ar. In contrast, it is 1.90 Ω cm^2 for LSCrF and 0.88 Ω cm^2 for LSCrFF in 3% H_2O/Ar. The low-frequency arcs (R_2) of cells based on LSCrF and LSCrFF correspond to dissociative adsorption, the transfer of species at TPB, and the

dx.doi.org/10.1021/am4020132 | ACS Appl. Mater. Interfaces 2013, 5, 8553−8562

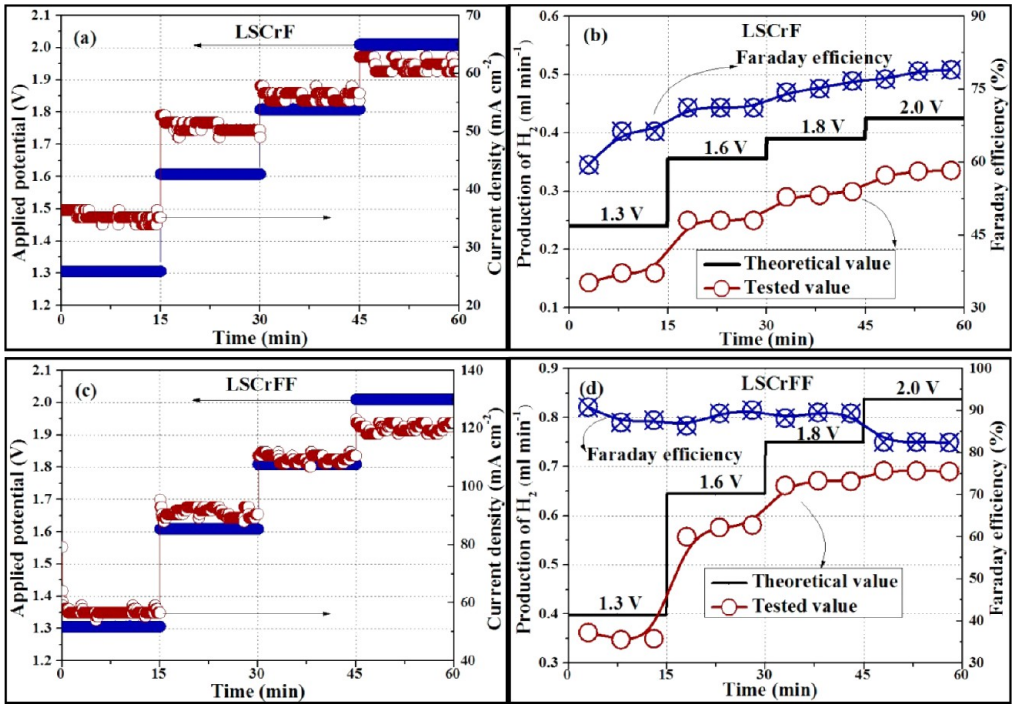

Figure 13. Electrolysis performance of the solid oxide electrolyzers with cathodes based on LSCrF and LSCrFF at different applied potentials of 1.3 V, 1.6 V, 1.8 V, and 2.0 V in 3% H_2O/Ar at 800 °C.

conversion process, which has become dominant. It was observed that the two arcs exist together over the range of 0−2.0 V of the applied potentials as illustrated in Figure 11, which implies that the electrochemical reduction of LSCrF and LSCrFF still exist at high voltages. However, the low frequency arcs become smaller as the voltage increases, indicating that the electrochemical reduction of cathodes is no longer the main limitation of the steam electrolysis, which has become the dominant process at higher potentials.

Solid oxide electrolyzers based on LSCrF and LSCrFF cathodes fed with 3% H_2O/4.93% H_2/Ar were performed for direct electrolysis of steam at 800 °C, and the profiles are as shown in Figure 12. For the cell based on LSCrF, the hydrogen generation from steam electrolysis increases with increasing current densities and reaches 0.31 mL min^{-1} at 61.6 mA cm^{-2}. However, the hydrogen production is higher for LSCrFF at all the corresponding potentials due to the improved electrocatalytic activity of cathode with anchored iron nanoparticles. On the other hand, the Faraday efficiency for the cell based on LSCrFF is rather higher with all potentials in contrast to the bare LSCrF cathodes. The iron nanoparticles largely improve the conversion process and extend TPB for the production of hydrogen. Also, the current efficiency is remarkably enhanced by approximately 28% for cell based on LSCrFF in comparison with LSCrF at low voltages in 3% H_2O/4.93% H_2/Ar.

In order to study the performance of the solid oxide electrolyzers with LSCrF and LSCrFF cathodes without a flow of hydrogen, both cells were operated with the cathodes in 3% H_2O/Ar at 800 °C. Figure 13 revealed that the current density of the cell based on LSCrFF (~120 mA cm^{-2}) is almost double that obtained for cell based on LSCrF (~63 mA cm^{-2}). This striking observation may be due to the enhancement of cathode performance with iron nanoparticles. The current efficiencies are accordingly higher for the cell based on LSCrFF with all potentials in contrast to the cell based on LSCrF with cathodes in 3% H_2O/Ar. Although, a decrease in Faraday efficiencies was also observed with potentials below 2.0 V for the cell based on LSCrFF; however, the efficiencies are still enhanced by ~21.3% when compared to the cell based on LSCrF with a potential between 1.3 and 1.6 V.

4. CONCLUSIONS

The reversible exsolution of iron nanoparticles anchored on the surface of the A-site deficient and B-site doped lanthanum chromate has been successfully achieved and utilized for the direct steam electrolysis. The electrical and electrochemical properties of LSCrFF and Fe/LSCrF were systematically investigated. The electrode polarization resistance of the symmetrical cells was enhanced from 4.26 Ω cm^2 with LSCrF cathode to 2.58 Ω cm^2 with Fe/LSCrF in hydrogen at 800 °C. The current densities were enhanced by ~50% with the loading of iron nanoparticles under the same potentials for direct steam electrolysis. More importantly, the current efficiencies were further enhanced by approximately 21% in a wide range of applied potentials. Overall, this study demonstrates that the synergetic effect of catalytically-active iron nanoparticles and a redox-stable LSCrF cathode leads to the improved composite cathode performances for direct steam electrolysis.

■ ASSOCIATED CONTENT

Supporting Information

Schematic of testing conditions, polarization resistance at hydrogen partial pressure for symmetrical cells based on LSCrF and LSCrFF, and the conductivity versus temperature of LSCrF and LSCrFF at 10^{-20} atm in 5% H_2/Ar. This material is available free of charge via the Internet at http://pubs.acs.org.

■ AUTHOR INFORMATION

Corresponding Authors

*E-mail: xiekui@hfut.edu.cn.

*E-mail: ycwu@hfut.edu.cn.

Notes

The authors declare no competing financial interest.

REFERENCES

(1) Karczewski, J.; Bochentyn, B.; Molin, S.; Gazda, M.; Jasinski, P.; Kusz, B. *Solid State Ionics* **2012**, *221*, 11−14.
(2) Hauch, A.; Ebbesen, S. D.; Jensen, S. H.; Mogensen, M. *J. Mater. Chem.* **2008**, *18*, 2331−2340.
(3) Yang, X. D.; Irvine, J. T. S. *J. Mater. Chem.* **2008**, *18*, 2349−2354.
(4) Xie, K.; Zhang, Y. Q.; Meng, G. Y.; Irvine, J. T. S. *Energy Environ. Sci.* **2011**, *4*, 2218−2222.
(5) Li, S. S.; Li, Y. X.; Gan, Y.; Xie, K.; Meng, G. Y. *J. Power Sources* **2012**, *218*, 244−249.
(6) O'Brien, J. E.; McKellar, M. G.; Stoots, C. M.; Herring, J. S.; Hawkes, G. L. *Int. J. Hydrogen Energy* **2009**, *34*, 4216−4226.
(7) Xie, K.; Zhang, Y. Q.; Meng, G. Y.; Irvine, J. T. S. *J. Mater. Chem.* **2011**, *21*, 195−198.
(8) Jensen, S. H.; Sun, X.; Ebbesen, S. D.; Knibbe, R.; Mogensen, M. *Int. J. Hydrogen Energy* **2010**, *35*, 9544−9549.
(9) Li, S. S.; Xie, K. *J. Electrochem. Soc.* **2013**, *160*, F224−F233.
(10) Udagawa, J.; Aguiar, P.; Brandon, N. P. *J. Power Sources* **2008**, *180*, 46−55.
(11) Ni, M.; Leung, M. K. H.; Leung, D. Y. C. *Electrochim. Acta* **2007**, *52*, 6707−6718.
(12) Pihlatie, M. H.; Frandsen, H. L.; Kaiser, A.; Mogensen, M. *J. Power Sources* **2010**, *195*, 2677−2690.
(13) Othman, M. H. D.; Droushiotis, N.; Wu, Z. T.; Kelsall, G.; Li, K. *Adv. Mater.* **2011**, *23*, 2480−2483.
(14) Atkinson, A.; Barnett, S.; Gorte, R. J.; Irvine, J. T. S.; Mcevoy, A. J.; Mogensen, M.; Singhal, S. C.; Vohs, J. *Nat. Mater.* **2004**, *3*, 17−27.
(15) Cowin, P. I.; Petit, C. T. G.; Lan, R.; Irvine, J. T. S.; Tao, S. W. *Adv. Energy Mater.* **2011**, *1*, 314−332.
(16) Konysheva, E. Y.; Xu, X. X.; Irvine, J. T. S. *Adv. Mater.* **2012**, *24*, 528−532.
(17) Gan, Y.; Zhang, J.; Li, Y. X.; Li, S. S.; Xie, K.; Irvine, J. T. S. *J. Electrochem. Soc.* **2012**, *159*, F1−F5.
(18) Plint, S. M.; Connor, P. A.; Tao, S. W.; Irvine, J. T. S. *Solid State Ionics* **2006**, *177*, 2005−2008.
(19) Oishi, M.; Yashiro, K.; Sato, K.; Mizusaki, J.; Kawada, T. *J. Solid State Chem.* **2008**, *181*, 3177−3184.
(20) Xu, S. S.; Chen, S. G.; Li, M.; Xie, K.; Wang, Y.; Wu, Y. C. *J. Power Sources* **2013**, *239*, 332−340.
(21) Xu, S. S.; Li, S. S.; Yao, W. T.; Dong, D. H.; Xie, K. *J. Power Sources* **2013**, *230*, 115−121.
(22) Tao, S. W.; Irvine, J. T. S. *Chem. Mater.* **2004**, *16*, 4116−4121.
(23) Danilovic, N.; Vincent, A.; Luo, J. L.; Chuang, K. T.; Hui, R.; Sanger, A. R. *Chem. Mater.* **2010**, *22*, 957−965.
(24) Li, Y. X.; Zhou, J. E.; Dong, D. H.; Wang, Y.; Jiang, J. Z.; Xiang, H. F.; Xie, K. *Phys. Chem. Chem. Phys.* **2012**, *14*, 15547−15553.
(25) Gong, Y. H.; Ji, W. J.; Xie, B.; Wang, H. Q. *Solid State Ionics* **2011**, *192*, 505−509.
(26) Zhu, Q. S.; Fan, B. A. *Solid State Ionics* **2005**, *176*, 889−894.
(27) Leng, Y. J.; Chan, S. H.; Khor, K. A.; Jiang, S. P.; Cheang, P. *J. Power Sources* **2003**, *117*, 26−34.
(28) Cho, S.; Kim, Y. N.; Kim, J. H.; Manthiram, A.; Wang, H. Y. *Electrochim. Acta* **2011**, *56*, 5472−5477.
(29) Choi, J. J.; Choi, J. H.; Ryu, J.; Hahn, B. D.; Kim, J. W.; Ahn, C. W.; Yoon, W. H.; Park, D. S. *J. Eur. Ceram. Soc.* **2012**, *32*, 3249−3254.
(30) Ramos, T.; Carvalho, M. D.; Ferreira, L. P.; Cruz, M. M.; Godinho, M. *Chem. Mater.* **2006**, *18*, 3860−3865.